Acta Materialia 148 (2018) 1–13

Contents lists available at ScienceDirect

Acta Materialia

journal homepage: www.elsevier.com/locate/actamat

Full length article

Strong composition dependence of resistive switching in $Ba_{1-x}Sr_xTiO_3$ thin films on semiconducting substrates and its thermodynamic analysis

O. Mohammadmoradi [a], C. Sen [a], A.G. Boni [b], L. Pintilie [b], I.B. Misirlioglu [a, c, d, *]

[a] Faculty of Engineering and Natural Sciences, Sabancı University, Orhanlı/Tuzla, 34956 Istanbul, Turkey
[b] National Institute of Materials Physics, Atomistilor 105bis, Magurele, 077125 Romania
[c] Integrated Manufacturing Technologies Research and Application Center, Sabanci University, Tuzla, 34956 Istanbul, Turkey
[d] Sabancı University Nanotechnology Application Center, Orhanlı/Tuzla, 34956 Istanbul, Turkey

ARTICLE INFO

Article history:
Received 31 August 2017
Received in revised form
3 February 2018
Accepted 6 February 2018
Available online 14 February 2018

Keywords:
Ferroelectric films
Thermodynamic theory
Resistive switching
Electrical measurements

ABSTRACT

In this work, we report on the variability of the Schottky effect in solution processed $Ba_{1-x}Sr_xTiO_3$ films (BST, $x = 0$, 0.5) grown on 0.5% Nb doped $SrTiO_3$ substrates with top Pt electrodes (NSTO/BST/Pt). The films display leakage currents accompanied by varying degrees of hystereses in the current-voltage measurements. The magnitude of the leakage and hystereses depend on the Sr content. We focus on the current-voltage (I-V) behavior of our samples in the light of thermodynamic theory of ferroelectrics coupled with equations of semiconductors. Our calculations allowed us to unambigously determine the electronic character of the defects and related band bending effects in our samples. The extent of asymmetry and the hystereses in the I-V curves for $x = 0$ and 0.5 are shown to be controlled by the polarization in qualitative agreement with our calculations. Amplitude of the ferroelectric polarization, which is a function of composition here, has a strong impact on leakage currents in forward bias while this effect is much weaker under negative bias. The latter occurs as polarization pointing away from the NSTO semiconducting substrate causes depletion of carriers at the NSTO side of the NSTO/BST interface, increasing resistance to current flow through the stack. Such an occurence also increases the energy gap between the Fermi level and the conduction bands of the films, thereby reducing the bulk conduction through the film as well. The dependence of leakage currents on polarization direction points out to the possibility of a non-destructive read-out route in ferroelectric films much thicker than tunnel junctions.
© 2018 Acta Materialia Inc. Published by Elsevier Ltd. All rights reserved.

1. Introduction

Formation of a Schottky junction between a semiconductor and a metal depends on the metal work function and the Fermi level of the semiconductor. In the case of a wide bandgap polar semiconductor such as GaN, ZnO and alike, the inherent electric polarization of the semiconductor comes into play as an additional parameter as polarization charges near the metal/semiconductor interface can generate significant potential drops leading to band bending accompanied by carrier depletion/accumulation in these regions. Ferroelectrics (FEs) are similar to polar semiconductors in the sense that both possess a polarization in the absence of the field but with three major differences: FE polarization is switchable, appears along with a structural symmetry breaking transition at a critical temperature and is strongly coupled to electric fields whereas other polar semiconductors exhibit a fixed polarization simply due to asymmetric bond angles between anions and cations intrinsic to the crystal structure. The Schottky diode effect in a ferroelectric film can also be switchable leading to the phenomena of resistive switching. It is naturally observed to be much stronger in ferroelectric films than a regular leaky dielectric owing to the presence of the remnant polarization in the former. In fact, any ferroelectric film with asymmetric electrodes with at least one of which is a semiconductor is expected to exhibit resistive switching due to the considerable penetration of the electric field into the semiconductor electrode. This occurs so as the extent of screening of polarization charges can vary significantly depending on depletion or accumulation states caused by the direction of the

* Corresponding author. Faculty of Engineering and Natural Sciences, Sabancı University, Orhanlı/Tuzla, 34956 Istanbul, Turkey.
E-mail address: burc@sabanciuniv.edu (I.B. Misirlioglu).

https://doi.org/10.1016/j.actamat.2018.02.015
1359-6454/© 2018 Acta Materialia Inc. Published by Elsevier Ltd. All rights reserved.

ferroelectric dipoles.

That the ferroelectric polarization is switchable and sensitive to local electric and elastic strain fields as well as the non-linear dependence of polarization on applied bias renders a “ferroelectric Schottky junction” different from a classical Schottky junction. The Schottky effect and how ferroelectric polarization influences this was discussed in some detail as early as 1994 in Ref. [1]. One of the first reports discussing the hystereses in the I-V curves of FE submicron films was published in 1997 but mostly with qualitative arguments [2]. Another recent outcome of the continuing interest related to this topic has been the switchability of the electronic character of interfaces as recently reported in some works [3,4] and polarization induced self-doping effects [5]. It has been shown in Refs. [[2 and 3]] that the boundary conditions for polarization, i. e., how polarization terminates at an electrode interface can determine whether carriers from electronic defects from inside of the film will accumulate or deplete that interface. Such formations distinguish between whether the interface will have Schottky or Ohmic character and determine the conduction (leakage) currents, which are inevitable in almost all ferroelectric thin film systems. Emanating from the film fabrication conditions, there is always some amount of deviation from exact stoichiometry of the lattice that introduces into these systems p-type or n-type electronic defects such as oxygen vacancies, impurities and etc. Thus, leakage currents due to these defects almost always form a “background current” when identifying the switching currents. The leakage currents are also subject to the electronic nature of the film/electrode interfaces.

In the same context mentioned above, the dependence of the “conduction” currents on the direction of ferroelectric polarization along the film normal in a sandwich type capacitor stack has gained recent interest as this could be perceived as a method of a non-destructive read-out in ferroelectric memory development. Such an approach has been repeatedly mentioned and tested in a number of works [6–30]. Several of these works focus on ultra thin films acting, in a way, as tunnel junctions (due to their small thicknesses) and memristors [18] with tunable resistance. In thicker films (>8–10 nm) where quantum tunneling diminishes, one needs to consider bulk conductivity to be able to interpret the leaky behavior commonly observed in ferroelectric thin films. The bulk conductivity is expected to be a function of polarization direction inside the ferroelectric film as long as the finite screening effects at the film/electrode interfaces exist, a phenomena that has been overlooked. This is so because the only “intrinsic” source of electric field in a ferroelectric is the partially screened polarization charges at the interfaces where the termination of the dipole sequence occurs. We must mention here that we classify applied bias and work function asymmetry of the top/bottomelectrodes as well as charged defects and defects with inhomogeneous elastic strain fields as “extrinsic” sources of electric field. At low-to-moderate bias values, bulk controlled leakage occurring in relatively thick films (>8–10 nm) will depend on finite screening effects of polarization and its direction and can be understood by the changes in the slopes of the energy bands and their position with respect to the Fermi level. In a conventional sandwich type FE capacitor with at least one SC electrode, the electrostatics of the stack is strongly determined by the sign of the partially screened polarization charges at the SC interface that will induce band bending occurring inside the film. The depletion barrier potential at the FE/SC interface is another important parameter determining the extent of current flowing through the stack. An on/off current ratio of around 10^4 was reported by Zhang et al. in polycrystalline $BiFeO_3$ films [29] followed by Bai et al. reporting this value to be 850 in 150 nm thick Pb(Zr0.4Ti0.6)O3 films that exhibited good ferroelectric stability despite high leakage currents [31]. Bottom semiconductor oxide substrates were used in both works amplifying the on/off current ratio as a function of polarization direction.

In addition to electrode related effects, the directional dependence of bulk conductivity on polarization could also be a strong function of whether or not strong surface effects other than electrostatic ones dominate from the FE film side. Surface electric fields from possible surface reconstruction effects removing the degeneracy of the polarization can be one factor [32]. The former is namely due to “polarization boundary conditions (BCs)” while the electrode screening is solely comprising the external electrostatic BCs on the system. Strong surface effects introduced into the system via the polarization BCs can lead to additional carrier-redistribution as reported in prior works [4]. Although theoretically possible, these effects are quite tricky to test in experiments and distinguishing them from bulk related effects are non-trivial. Note that tunneling effects are outside of bulk conduction explained here as the existence of tunneling between local traps as a contribution to leakage is another possible mechanism but requires relatively high fields than considered herein this work.

Composition of ferroelectric films is often a parameter in tailoring a specific functionality towards a desired response in IC devices. As any “functional output” for any composition is sensed in terms of variations in currents generated by the stack in applications, leakage and mechanisms giving rise to these currents are of utmost importance. We shall show in this paper that leakage and its relation to polarization can be tailored to design stacks displaying resistive switching. In this paper, we report on the resistive switching effect that vary with Sr content in high quality (Ba,Sr)TiO_3 (BST) films that we fabricated via a solution precursor deposition method and analyze their current-voltage behavior in the light of thermodynamic theory of ferroelectrics. BST compositions offer the flexibility to design functionalities around the choice of the Sr content for a range of applications and particularly for agile dielectric tunable devices [33–38]. The major motivation behind this study was to investigate the effect of polarization strength on the leakage behavior of ferroelectric films where the (Ba,Sr)TiO_3 provides an ideal platform for this purpose. Polarization strength is expected to be a function of Sr content when grown on a compressive substrate such as $SrTiO_3$ and alter the leakage current magnitudes. Although we fabricated 3 compositions, namely $BaTiO_3$ (BT), $Ba_{0.7}Sr_{0.3}TiO_3$ (BST 7030) and $Ba_{0.5}Sr_{0.5}TiO_3$ (BST 5050), we compare the results from BT and BST 5050 as BST 7030 always falls into an almost average behavior of the two end compositions. Such an outcome is entirely consistent with the mechanisms we provide here to explain the compositional dependence of the current-voltage behavior we report for BT and BST 5050. We therefore find it sufficient to compare experimental results in the light of thermodynamic simulations for two compositions, namely BT and BST 5050, to reveal that the difference in the polarization strength would cause dramatic variations in the diode-like behavior. Following the experiments, we computed the band bending and carrier distribution maps in these compositions grown on conducting Nb:$SrTiO_3$ (NSTO) electrodes with top Pt electrodes using published phenomenological parameters for these materials including the NSTO. In the calculations no apriori assumptions were made and we discussed the asymmetry in the experimental current-voltage (I-V) and the capacitance-voltage (C-V) curves in the light of our results. The electronic defect type consideration in our thermodynamic approach confirms that all films in this work behave as n-type semiconductors with approx. volumetric impurity densities of about $10^{24}\,m^{-3}$.

2. Experimental method

In this study, BST films with two different compositions of (BT

and BST 5050) were prepared by the sol-gel method. The used chemicals were Barium Acetate (Ba $(AC)_2$) (Sigma-Aldrich), Strontium Acetate (Sr $(AC)_2$) (ABCR), Titanium (IV) Isopropoxide (TIP) (Sigma-Aldrich), Glacial Acetic Acid (GAA) (MERCK) and 2-Propanol (MERCK). In order to obtain the final solution from precursors films fabrication, two separate solutions were prepared. The first solution was made by mixing the Ba $(AC)_2$, Sr $(AC)_2$ with GAA. This solution was left for mixing on the stirrer for 1 h at room temperature. The second solution was prepared by mixing the TIP and 2-propanol on the stirrer for 30 min at room temperature. After 1 h, first solution was added to the second one and the whole mixture was stirred for 1 h at room temperature. The concentration of the obtained solution was 1 M. In order to deposit higher quality films, 0.5 M solution was prepared by diluting the 1 M solution via adding GAA. The detailed information about the mixing ratio and sample coding are presented in Table 1.

Prepared solutions were deposited on the substrates by spin coating method (Laurell spin coater model WS-650-23B). The spin speed and spin time were optimized in forms of two steps. In the first step, spin speed was set to 500 rpm for 15 s followed by another step at 6000 rpm for 60 s. Deposited films were dried in air at 200 °C for 5 min on hot plate. Then they were heated up to 400 °C by 5 °C/min rate and were are kept in 400 °C for 30 min. Samples were then heated up at the same rate to 800 °C and kept at this temperature for 150 min. The flowchart of the sample preparation process is given in Fig. 1. The entire heat treatment process (including heating up and cooling down) was carried out in an oxygen rich environment (2.0 l/min flow rate). The films were then characterized by XRD for structural information followed by Scanning Electron Microscopy (SEM) for morphological information.

The XRD patterns of the samples revealed that we obtained highly [001] textured films in both BT and BST 5050 (shown around the (002) substrate peak in Fig. 2) where the only peaks we observed exhibit a shallow hump centered around $2\theta = 45.4^\circ$ belonging to the (002) out-of-plane spacing of the tetragonal phase of BT. In the case of BST 5050 we only observed a slight change in intensity of the Nb:SrTiO3 shoulder near $2\theta = 46.3^\circ$ that is possibly due to the relatively low misfit of the BST 5050 with the underlying substrate. Despite its composition falling into the paraelectric regime at room temperature and absence of any compressive strong misfit, the latter still exhibits a clear ferroelectric behavior along the film normal as evidenced through the C-V measurements. The XRD pattern also included additional peaks due to diffraction of Cu $K_{\alpha 1}$ and $K_{\alpha 2}$ from the NSTO single crystal causing a splitting of the (002) peaks at $2\theta = 46.47^\circ$ and 46.59° respectively. A small intensity of Cu K_β diffraction from the (001), (002) planes were also detected at $2\theta = 20.53^\circ$ and 41.78 as labeled in Fig. 2. The NSTO substrate peaks are the ones with the high intensity at 22.74° and 46.45° respectively corresponding to (001) and (002) planes. No secondary phases were detected in the films and we also checked the stoichometry of our BT and BST 5050 films via carrying out an EDX analysis during SEM studies of the film morphologies. Due to the strong overlap between Ba Lα and Ti Kα peaks for an incident electron beam energy of 12 keV in addition to the strong substrate signal, the chemical composition analysis was not reliable. XRD patterns of the powders prepared from the same solution together with the film samples (not shown here) were used in estimating composition. We noted that the pattern of the BST 5050 composition was in fact matching the peak positions one would expect in a BST 4456 composition corresponding to a slightly higher Sr content than 0.5 (out of 1) at A-sites. The BT film proved to be in accordance with previously published JCPDS data [39]. In spite of the small composition difference mentioned above, we denote the BST composition as BST 5050 in the entire paper for convenience. Note that such a minor difference in composition has no effect on the underlying physics of the problem as well as the thermodynamic calculations.

Following the XRD experiments, circular shaped platinum (Pt) electrodes with 70 μm diameter and approx. 100 nm thickness were deposited on the films using a Torr Thermal evaporator. The electrical characterization was carried out at National Institute of Materials Physics (NIMP) in Bucharesti, Romania. The equipment at NIMP includes a Lakeshore cryoprober model CPX-VF, a Keithley electrometer model 6517 (for I–V characteristics), a ferroelectric tester model TF2000 from aixACCT (for hysteresis loops), and an impedance analyzer model HP 4194 A for C–V measurements. Two different configurations were used to carry out the electrical measurements whose schematics are provided in Fig. 3. The first configuration was used to obtain the I-V curves while the second configuration was used for C-V measurements for reduced leakage contribution in the latter.

3. Theoretical method

To shed light on the experimental observations, particularly the I-V curve asymmetry and the hystereses observed in these curves, we referred to the thermodynamic theory of ferroelectrics with appropriate modifications and considerations pertaining to the systems analyzed here. We provide a schematic of the BST heterostructures analyzed in this work in Fig. 4. The total thickness of the films are taken as 100 nm as this is approximately the thickness of the grown films. The material parameters of a given composition of $(Ba,Sr)TiO_3$ are assumed to be a weighted linear average of the constituents, namely BT and ST in the following manner:

$$s^f = (1\text{-}f) \cdot s^{BT} + f \cdot s^{ST} \quad (1)$$

where s^f is any material parameter, such as the band gap, thermodynamic stiffness coefficients, or unit cell lattice parameter of a film corresponding to a particular fraction of Sr replacing Ba ions in the lattice, namely f, s^{BT} and s^{ST} are any given material parameter for pure BT and ST, respectively. f is taken in this model as 0 and 0.5, corresponding to relevant bulk Curie temperatures and other coefficients of the films as prescribed above. Averaging of material properties, both thermodynamic, structural and electronic, is an approximation to serve as a means to provide us with the results that can be used to interpret certain electrical behavior observed in these structures. As the experiments show that compositions considered in this study, namely BT and BST 5050 are all in the ferroelectric phase on NSTO (Please see the experimentally obtained C-V plots in Fig. 5 where ferroelectric switching is evident from the so-called butterfly shape of the curves), we assign a small compressive misfit of −1% to each structure allowing us to treat all

Table 1
Chemical precursor mixing ratio for the fabrication of films used in this work.

Sample Code	Composition	Ba $(AC)_2$ (g)	Sr $(AC)_2$ (g)	GAA (mL)	TIP (mL)	2-Propanol (mL)
BT	$BaTiO_3$	2.5542	0	10	3	15.5
BST50/50	$Ba_{0.5}Sr_{0.5}TiO_3$	1.2771	1.0285	10	3	15.5

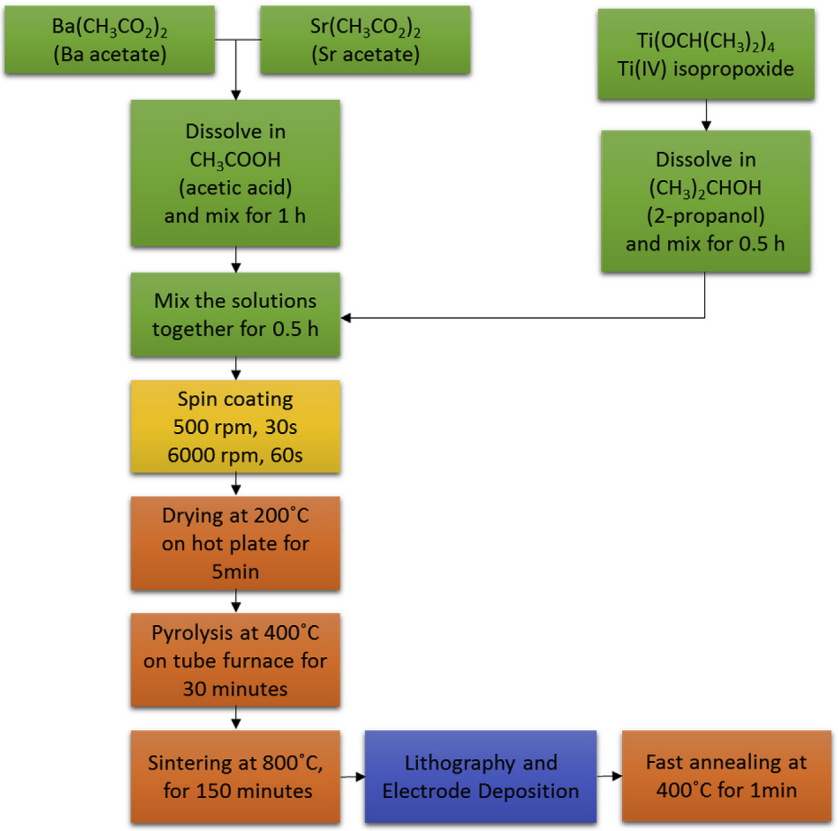

Fig. 1. Flow chart of thin film preparation in this work. The last rapid annealing stage is for the crystallization of the top electrodes.

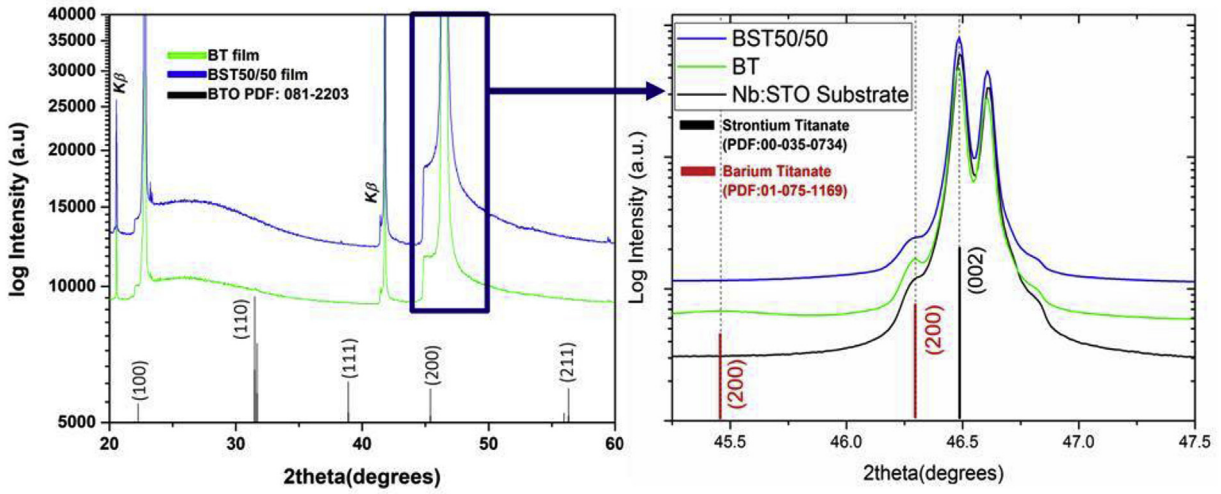

Fig. 2. The XRD patterns of the BT and BST 5050 films grown in this work. The region falling into the blue rectangle on the right plot is enlarged to reveal the (002) region of the substrate. The peaks labeled as K_β are a result of the Cu K_β radiation leaking from the X-ray tube and diffracting from the (100) and (200) planes of the films at $2\theta = 20.53^\circ$ and 41.78° respectively. No secondary or unidentified peaks are present, implying the high perovskite phase fraction in our samples. In the enlarged portion of the pattern around the substrate peaks, the high intensity dual peaks at 46.47° and 46.59° emanate from diffraction of $K\alpha 1$ ($1s - 2s$ transition) and $K\alpha 2$ ($1s - 2p$ transition) radiation of Cu from the (002) substrate planes. (002) of the BST 5050 is not visible implying a well matching of this composition with NSTO. BT film exhibits a slight hump around its bulk (002) peak position near 45.5° indicating some degree of relaxation from the -2.56% misfit with the NSTO. (For interpretation of the references to color in this figure legend, the reader is referred to the Web version of this article.)

compositions in their respective ferroelectric regimes. How this misfit aids in obtaining ferroelectricity shall be shown in the coming paragraphs of this section. In a polar dielectric sandwiched between a semiconductor and an electrode, the Maxwell equation

$$\nabla \cdot \vec{D} = \rho \tag{2}$$

has to be satisfied at every point in both films, with any composition, deposited on bottom n-type NSTO electrode considered here.

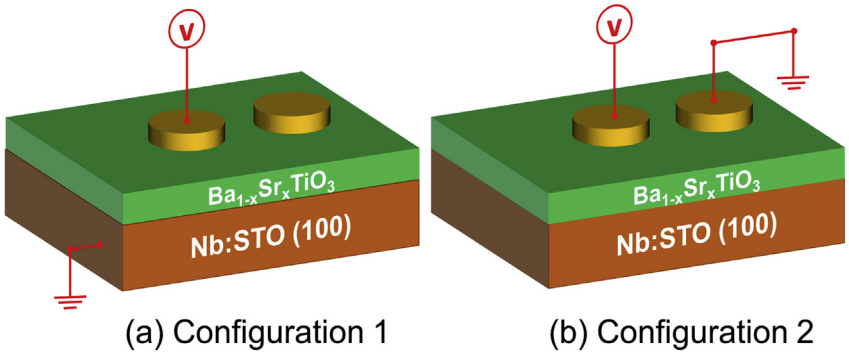

Fig. 3. The 2 configurations of electrical measurements pursued in this work: (a) through-thickness measurement and (b) capacitors in series measurement to get the C-V curves.

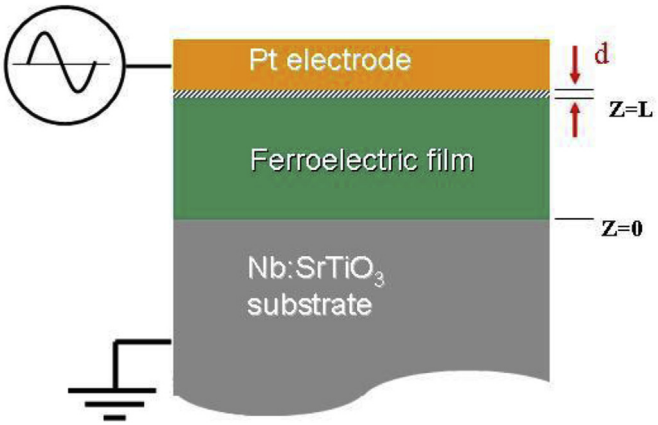

Fig. 4. The schematic of the stack used in the thermodynamic calculations. Shaded region at the Pt/film interface indicates the presence of a dead layer whose thickness is d (taken as 0.5 nm in our work). The details of the boundary conditions are defined in Sect. 3.

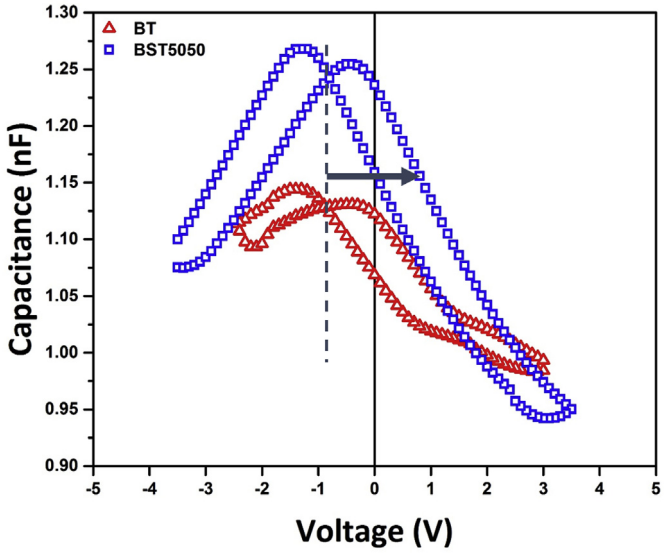

Fig. 5. C-V curves obtained from configuration 2 in this work for BT and BST 5050 films.

One can suppose that the top metal electrode (Pt here) does not allow any field penetration (ideal electrode behavior), although this assumption has to be modified to some extent for finite screening considerations as will be shown. We can write $\vec{D}$, the dielectric displacement vector, as

$$\vec{D} = [D_x\hat{x} + D_z\hat{z}] \tag{3}$$

where

$$D_x = \varepsilon_o\varepsilon_b E_x + P_x \text{ and } D_z = \varepsilon_o\varepsilon_b E_z + P_z \tag{4}$$

in the FE layer with x and z denoting the in-plane and out-of-plane components respectively and,

$$D_x = \varepsilon_0\varepsilon_r E_x \text{ and } D_z = \varepsilon_0\varepsilon_r E_z \tag{5}$$

in the n-type bottom electrode having a dielectric constant of $\varepsilon_r$taken as that of undoped $SrTiO_3$ ($\approx$300). In Eqs. (4) and (5), ε_o is the permittivity of the vacuum and ε_b is the background dielectric constant of the FE (10 in this work, see Refs. [40,41] for its explanation), E_x and E_z are respectively the$x-$ and $z-$ components of the electric field vector $\vec{E}$ determined from $E_x = -\partial\phi/\partial x$ and $E_z = -\partial\phi/\partial z$, P_x and P_z are the FE polarization components along x- and z-axes respectively. ρ is the total charge density and consists of electrons, holes and ionized donors in the n-type NSTO bottom electrode and donor impurities in the FE:

$$\rho = q\left(-n^- + p^+ + N_D^+\right) \tag{6}$$

where

$$N_D^+ = N_D\left[1 - \left(\exp\left(\frac{q(E_D - E_F - \varphi)}{kT}\right) + 1\right)^{-1}\right] \tag{7}$$

$$n^- = N_C\left(\exp\left(\frac{q(E_C - E_F - \varphi)}{kT}\right) + 1\right)^{-1} \tag{8}$$

$$p^+ = N_V\left[1 - \left(\exp\left(\frac{q(E_V - E_F - \varphi)}{kT}\right) + 1\right)^{-1}\right] \tag{9}$$

N_D^+ (N_D) is the ionized (total) donor density either in the n-type bottom electrode or the FE film. N_D can be expressed as $N_D = N_{BE} + N_{FE}$ where N_{BE} stands for the volumetric density of doping in the bottom oxide electrode, namely Nb concentration in $SrTiO_3$ and N_{FE} denotes the n-type impurity concentration in the $(Ba,Sr)TiO_3$ layer, n^- is the electron density, $p^+$is the hole density, N_C is the effective density of states at the bottom of the conduction band, N_V is the effective density of states at the top of the valence band, E_C is the energy of an electron at the bottom of the conduction band, E_V is

the energy of an electron at the top of the valence band at a given coordinate (either the FE film or the NSTO), E_F is the Fermi level, φ is the local electrostatic potential. All the band parameters for NSTO and BST 5050 are given in Table 2. To carry out the calculations including the band bending in the stack, one needs to know E_F of the stack. Assuming the large volume of the NSTO compared to the film and the electrode volumes, we suppose that the bottom conducting oxide electrode acts as a carrier reservoir and that the Fermi level of the stack equilibriates with that of the bottom substrate acting as a carrier reservoir due to its large volume compared to the film and the Pt top electrode. Electrostatic (for the potential) and non-electrostatic boundary conditions (for the polarization) are needed to obtain solutions to the above equations. The boundary conditions for the electrostatic potential are:

$$\varphi_{FE} = \varphi_{nSC} @ z = 0 \tag{10}$$

implying the continuity of the potential at the FE/nSC interface, whereφ_{FE} and φ_{nSC} are the electrostatic potentials inside the FE and the n-type NSTO bottom electrode respectively, and

$$\varphi_{FE} = \varphi_{DL} = 0 @ z = L + d \tag{11}$$

at the FE/metal interface, where we assumed the presence of a thin dead layer ($d = 0.5$ nm thick) having a dielectric constant of 70 that is approx. the "background lattice polarizability" of the Pt metal as reported earlier [43], φ_{DL} denotes the potential in this layer that is to be computed from $\nabla \cdot D_{DL} = 0$ where subscript "*DL*" stands for "dead layer" and components of D has their usual meaning as in Eq. (5). The bias is always applied to the top Pt electrode, and the bottom conducting oxide electrode is always kept at zero potential (implying this electrode is grounded similar to the experiment). Periodic boundary conditions (BCs) are employed along the plane of the structures for both the electrostatic potential and polarization. While the electric field is connected to the dielectric properties of the nSC bottom electrode and FE via Eqs. (3) and (4), Landau-Ginzburg Eqs. of state for polarization also have to be satisfied in the FE layer:

$$2\alpha_3^m P_z + 4\alpha_{13}^m P_z P_x^2 + 4\alpha_{33}^m P_z^3 + 6\alpha_{111} P_z^5 + \alpha_{112}\left(4P_z P_x^4 + 8P_z^3 P_x^2\right) + 2\alpha_{123} P_z P_x^4 - G\left(\frac{\partial^2 P_z}{\partial z^2} + \frac{\partial^2 P_z}{\partial x^2}\right) = -\frac{\partial \varphi}{\partial z} \tag{12}$$

Table 2
Phenomenological constants and band parameters used in the calculations.

	$SrTiO_3$ [52]	$BaTiO_3$ [44]
Lattice parameter (nm)	0.3904	0.4004
T_C (°C)	−253	130
C (10^5 °C)	8×10^5	1.5×10^5
α_{11}(N m^6/C^4)	6.8×10^9	$3.6 \times (T\text{-}175) \times 10^8$
α_{12}(N m^6/C^4)	2.74×10^9	-0.0345×10^8
α_{111}(N m^{10}/C^6)	0	6.6×10^9
α_{112}(N m^{10}/C^6)	0	18.14×10^8
α_{123}(N m^{10}/C^6)	0	-7.45×10^9
S_{11}(10^{-12} N/m^2)	5.546	8.3
S_{12}(10^{-12} N/m^2)	−1.562	−2.7
S_{44}(10^{-12} N/m^2)	9.24	9.24
Q_{11}(m^4/C^2)	0.0457	0.11
Q_{12}(m^4/C^2)	−0.0135	−0.043
Q_{44}(m^4/C^2)	0.00975	5.165×10^{-2}
g (10^{-10} J m^3/C^2)	6 [53]	6 [53]
N_V, N_C (m^{-3})	10^{25}, 10^{25}	10^{25}, 10^{25}
E_V, E_C, E_D (eV)	−7.1, −3.9, −4.0	−6.72,-4.0,-4.1

$$2\alpha_1^m P_x + 2(2\alpha_{11}^m + \alpha_{12}^m)P_x^3 + 2\alpha_{13}^m P_x P_z^2 + 6\alpha_{111} P_x^5 + 2\alpha_{112}\left[3P_x^5 + 3P_x^3 P_z^2 + P_x P_z^4\right] + 2\alpha_{123} P_x^3 P_z^2 - G\left(\frac{\partial^2 P_x}{\partial z^2} + \frac{\partial^2 P_x}{\partial x^2}\right) = -\frac{\partial \varphi}{\partial x} \tag{13}$$

subject to the BCs in Eq. (14). Here α_3^m, α_{13}^m, α_{33}^m, α_1^m, α_{11}^m, α_{12}^m are the renormalized phenomenological thermodynamic coefficients [44] in SI units with α_1^m and α_3^m being $\alpha_1^m = \alpha(T - T_C) - u_{ij}^M(Q_{11} + Q_{12})/(S_{11} + S_{12})and\alpha_3^m = \alpha(T - T_C) - 2u_{ij}^M Q_{12}/(S_{11} + S_{12})$ due to renormalization with misfit strain where $\alpha = (2\varepsilon_0 C)^{-1}$, α_{12}^m and α_{33}^m contain the clamping effect of the film, while α_{111}, α_{112}, α_{123} are the dielectric stiffness coefficients in the bulk and are computed as defined in Eq. (1) for BT and BST 5050, u_{ij}^M is the misfit strain tensor for a cubic structure and is taken here as −1% (negative here meaning compression) that keeps the FE polarization along the normal of the stack plane both in BT and BST 5050 as the experiments reveal ferroelectricity in both samples along the film normal. G is the gradient energy coefficient and is assumed to be isotropic for convenience. All the phenomenological coefficients used in the thermodynamic calculations are provided in Table 2. The polarization boundary conditions at the m/FE and FE/nSC interfaces are important as previously discussed [4,45] and can be expressed as

$$\left[P_z + \lambda \frac{dP_z}{dz}\right]_{z=0,L} = 0, \quad \left[P_x + \lambda \frac{dP_x}{dz}\right]_{z=0,L} = 0 \tag{14}$$

with z indicating the coordinates for m/FE and FE/nSC interfaces, $\lambda$is the extrapolation length determining the extent of the change of polarization along the film normal at the interface and is a parameter implying how polarization terminates at the interfaces (taken as 3 nm here based on previous reports [46]). We employ a finite difference discretization in 2D and carry out a Gauss-Seidel iterative scheme to solve the coupled Eqs. (1) and (2) and (6)–(9) 2-13 simultaneously subject to BCs in Eqs. (10), (11) and (14). The computation grid consists of nh x 200 points where h is the distance between the nearest nodes both along x- and z-axes with a value equal to the cubic state of the FE (~4 Å), where n is the number of nodes whose sum gives the FE layer thickness (100 nm as aforementioned). We terminate the solution after 5000 iterations that yield a difference of about 10^{-4} for P between two consecutive steps. All results here are provided for room temperature calculations.

4. Results and discussion

Our attempts to obtain the polarization-electric field (P-E) hysteresis curves to confirm the ferroelectricity in our samples were inconclusive due to the large amounts of leakage currents. When obtaining the P-E plots of the BT and BST 5050 films, we chose ±3 V and ±4 V respectively for each sample as we did not want to push the samples into the high leakage current regime but the hystereses loops were still bloated. As we shall show later in the paper, BT in particular is vulnerable to leakage at bias values exceeding ±2 V. Following this, we conducted capacitance-voltage (C-V) measurements at 1 kHz where the ferroelectric switching peaks in capacitance are clearly observed in both BT and BST 5050 compositions, confirming room temperature ferroelectricity in the samples (See Fig. 5). The fact that BT has lower capacitance compared to BST 5050, especially near zero bias, is likely related to the larger misfit strain of this composition with the NSTO substrate in addition to its inherently higher Curie temperature. Looking at

the XRD pattern in Fig. 2, BT film has a slight hump around 45.5°, a possible outcome of a small portion of this film having structural variants and higher defect density due to strain relaxation. It must be kept in mind that spin coated samples do not reach the quality level of pulsed-laser deposition or similar plasma based vacuum deposition techniques but electronic character and behavior of the interfaces are often weakly dependent on microstructure for an average quality film that homogeneously covers the substrate. Overall, one might expect to have higher density of structural defects in BT than in BST 50/50, causing the relative detoriation in the C-V response. Close to zero bias capacitance, as BT is strained more than BST 5050 (compressively), it is feasible to expect BT to have a higher Curie temperature than that of BST 5050, leading to a lower capacitance in the former in all bias range, consistent with the thermodynamic theory of these compositions.

We already explained in the Experimental Section that the C-V curves were extracted in a "capacitors in series" mode measurement where we benefit from 2 blocking interfaces that lowers the leakage current flowing through the system (Fig. 3b), allowing us to go up to ±3 V in the BT film. The shift of the C-V curves towards the negative bias voltages in both samples is due to the asymmetry of the top/bottom electrodes in addition to carrier depletion/accumulation at the electrode interfaces as will be discussed in the coming paragraphs. Note that, if the data were to be plotted in terms of the electric field, this would have meant a shift towards a positive field axis as $E_z = -\partial\varphi/\partial z$(See Fig. 5). The up-sweep bias and down-sweep bias curve forms are quite symmetric and do not reveal directly any Schottky diode effects as one might expect depletion/accumulation states either in the film or the FE/NSTO interface that would alter the capacitance behavior at the relevant applied bias values.

Frequency dependent and quasi-static current-voltage curves in both the BT and BST 5050 samples reveal a hysteresis at both polarities as provided in Fig. 6. That the hystereses in the I-V curves occur in both 1 kHz signal and the quasi-static bias sweep means this behavior is not related to any dynamic effects, carrier trapping defects or delays such as dielectric relaxation processes and similar. The possible deep trap effects could also be expected to produce a hysteresis in a dynamic I-V measurement on the positive bias side but the up-sweep (from zero bias) would yield the upper branch of the hysteresis and the down sweep (to zero bias) would form the lower branch, just the opposite of what we observe in our samples. The hystereses in the negative bias regime, on the other hand, can be attributed to dynamical effects or trap related phenomena in the 1 kHz measurements as no such effect is present in the negative bias regime of the quasi-static I-Vs (Compare Fig. 6a and b). Trap driven phenomena often reveals itself in frequency dependent measurements and is unlikely to be observed in quasi-static measurements (due to trap relaxation). The disappearance of the hystereses on the negative bias side of our films when switching from the 1 kHz dynamical measurement to the quasi-static measurement is perfectly according with this definition. On the other hand, we see the hystereses in both dynamical measurements and quasi-static measurements for positive bias side, a strong implication of dependence of currents on polarization direction. In fact, the hystereses in our I-V experiments get much more prominent in quasi-static measurements, just the opposite of what one would expect from trap driven effects.

The currents recorded during the positive and negative bias sweeps (See Fig. 7) are also quite different in magnitude that can be explained qualitatively by the diode-like behavior. In a ferroelectric, however, the presence of polarization can significantly alter this outcome and the results need to be evaluated considering the presence of a switchable spontaneous electric polarization. The smearing of the "current curves" in Fig. 7 especially in the negative bias regime of the BT is pointing out to a "more difficult and gradual" switching as well as increased resistance in the NSTO/BT/Pt samples for negative polarity. This effect in BST 5050 is not as prominent as that of what we observe in BT. This can be explained on the basis of the difference in the amplitude of the polarization in the two samples where a weaker polarization (in BST 5050) is expected to induce a shorter depletion length in the NSTO as we shall discuss in the next paragraph.

Switching in a ferroelectric proceeds by nucleation of domains of opposite polarization sign and growth of these regions as long as the bias favoring the nucleated domains is kept on the system. Locally nucleated domains will require compensation of the bound polarization charges at least from the electrode side to overcome the depolarizing fields they are experiencing (hence the FE/electrode interfaces being likely sites for domain nucleation and

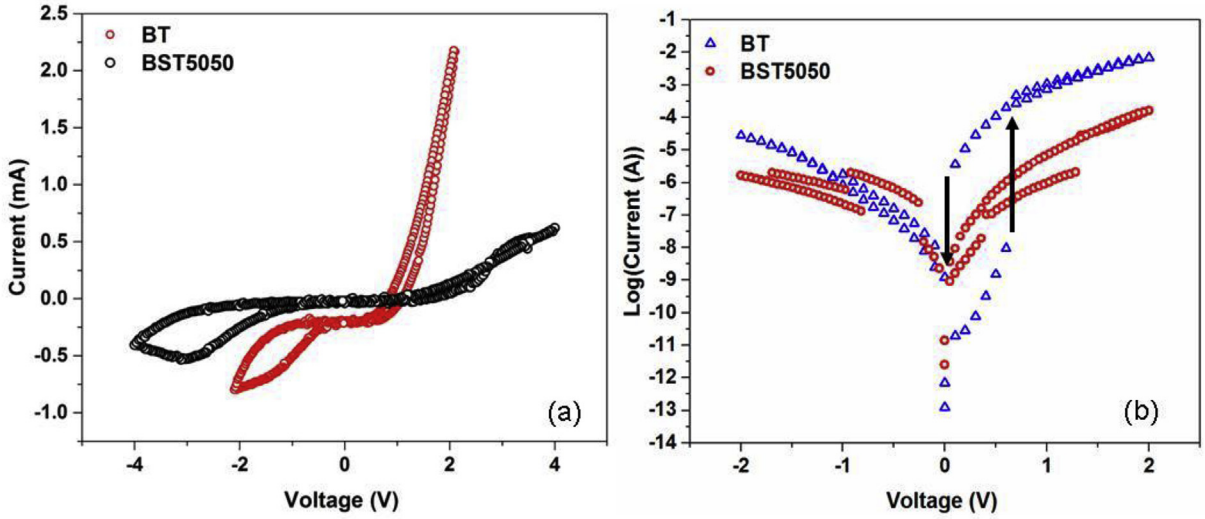

Fig. 6. I-V curves obtained from (a) 1 kHz dynamic and (b) quasi-static measurements in BT and BST 5050 films. Notice the hystereses in the positive bias regime of the BT. The up arrow indicates the jump in conductivity at the bias when polarization switches and starts pointing towards the NSTO interface while applying positive bias to top electrode. The arrow pointing down near zero bias indicates diminishing current while approaching zero bias after the max positive bias was already applied.

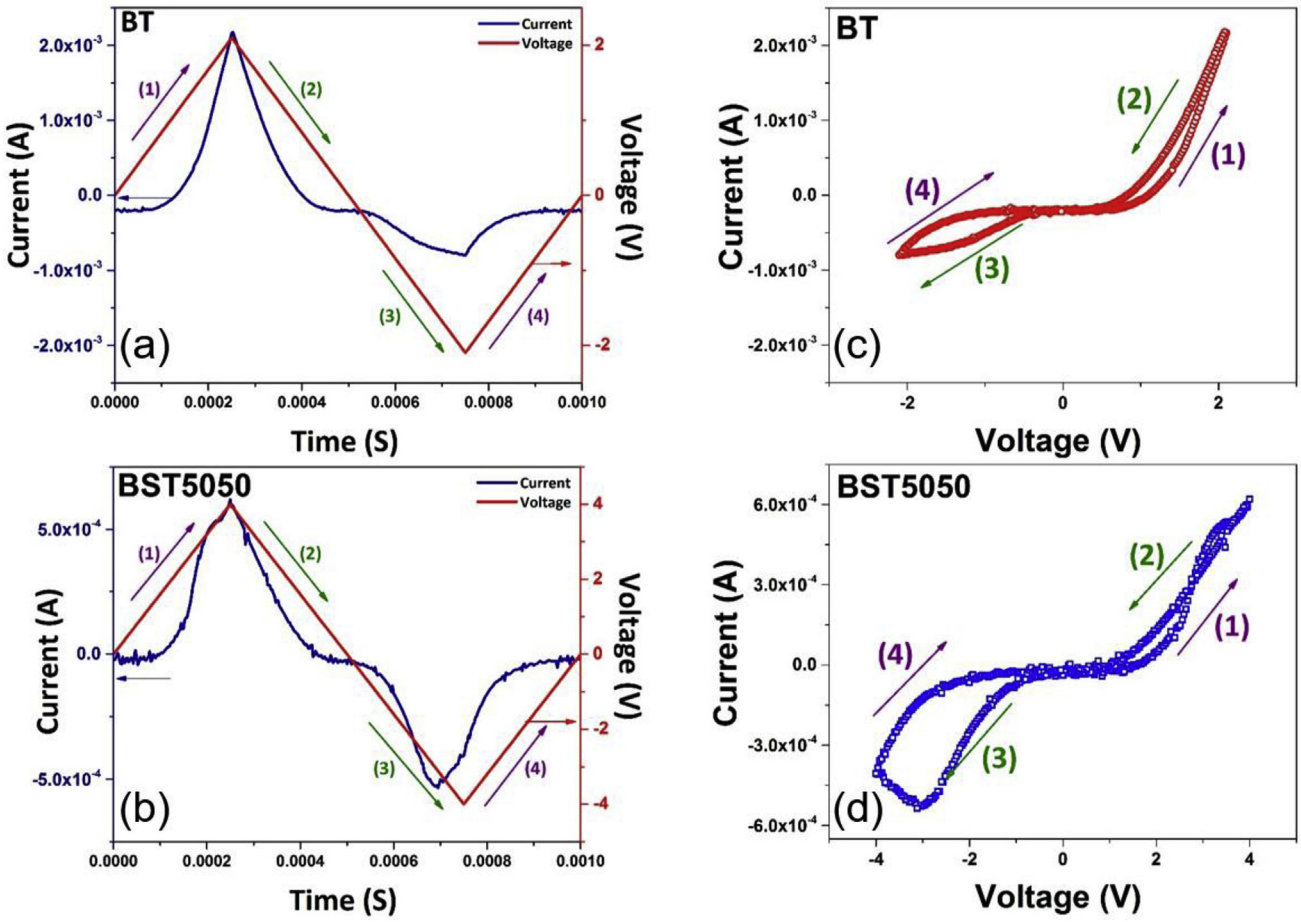

Fig. 7. Variation of the currents during the dynamic sweep in (a) BT and (b) BST 5050 samples and the corresponding I-V loops are provided in (c) and (d) respectively. Note that the currents in BT are considerably greater than that of BST 5050 especially in the positive bias regime.

growth). As the polarization strength of BT is expected to be higher than that of the BST 5050, a greater length of depletion occurs at the BT/NSTO interface, whereby the newly nucleated domains near this interface are screened only by fixed ionized donors instead of free carriers, making switching under negative bias more difficult and gradual. This "carrier depleted" state on the bottom electrode while polarization is still pointing away also reduces the overall current passing through the stack during application of bias, hence the behavior given in Fig. 7a is observed. Note that, despite the smaller polarization strength in the BST 5050 films, hence smaller depletion lengths on the NSTO side for these samples, the overall current on the negative bias regime is relatively comparable to that of BT or perhaps slightly more (when corrected for the shift in current towards negative values near zero bias). This supports the view that it is the unsufficient screening and presence of a depletion layer at the FE/NSTO interface that leads to a more difficult switching, reducing and smearing the currents for negative bias. The effect is most pronounced in BT as one expects greater depolarizing fields for films of this composition in the presence of a semiconducting bottom electrode.

Thus, the increased resistance of the BT samples to current flow when under negative bias (and partly under positive bias before polarization switching takes place, see the lower portion of the I-V curve for BT in Fig. 6b until around 0.75 V) can qualitatively be explained on the basis of the "depletion of carriers" at the NSTO side of the NSTO/FE interface. The mechanism by which this occurs needs further elaboration, particularly due to the presence of polarization and its strength. To do so, we refer to the results we obtained using the theoretical method prescribed in Section 3 under various bias values. Zero bias polarization and charge density maps indicate that the samples are expected to be "up polarized" that is consistent with the shift along the bias axis in the experimental C-V curves as well as the I-V curves as will be shown. Refering to our experimental data, we note that I-V curves especially in BT start at high resistance state corresponding to the polarization pointing away from the FE/NSTO interface. The "polarization pointing up" state does not change with until around 0.75 V for BT films, and 0.5 V for BST 5050. We shall later on demonstrate that this is consistent with the thermodynamic computation results. Note that the bias values are always assigned to the top Pt electrode (See Fig. 4). We again would like to remind here that we carried out the calculations without any assumptions regarding the built-in bias in the stacks or additionally "inserted" conditions and are thus qualitatively very useful to shed light on the experimental data.

In all the simulations, we assumed a n-type impurity density of 10^{24} m^{-3} in the films as such densities are often reported in similar perovskite ferroelectrics and used in other computational studies [47–49]. This is also required, in fact, to be able to simulate leaky films with the bloated hystereses behavior. That we consider n-type impurities is consistent with the Schottky behavior observed in our experiments with $\varphi_{NSTO} > \varphi_{FE}$ where FE is either BT or BST 50/50. We find that the positive, imprinted polarization direction leads to considerable electron depletion on the NSTO electrode near the

NSTO/FE interface even at zero bias both in BT and BST 5050 with the latter having weaker electric fields (due to weaker polarization) with less penetration into the conducting NSTO as expected (Fig. 8). In general, when the negative monopole of the ferroelectric dipoles point towards the bottom NSTO electrode, the carriers in the NSTO are repelled from the interface, exposing the ionized Nb donors that are fixed in their lattice coordinates. Negative bias only amplifies this effect, i. e., the depletion zone in the NSTO grows with bias increasing in the negative direction (not shown here). A similar observation was reported in Ref. [50] in $BiFeO_3$ films with electrical domains on $La_{0.67}Sr_{0.33}MnO_3$ electrodes and we should add here that such an outcome is a combined effect of bottom electrode and band bending effects inside of the ferroelectric film. Periodic band bending schemes in the presence of electrical domains were discussed in a recent work [51]. Thus, for "upward polarization" the polarization charges are screened via "fixed space charges" from the NSTO side at the NSTO/BT (or BST 5050 albeit a weaker polarization) interfaces at zero bias, any negative bias and, in fact, even in slightly positive bias before polarization switching takes place (≈ 0.5 V), hence the hystereses in the I-V curves of these systems. The presence of the space charge (carrier depleted) region at the NSTO side of the stack is a "high resistance" region that lowers the amount of current passing through the stack in the limit of the NSTO/DZ/FE/Pt stack acting as a "resistors in series" where the "DZ"

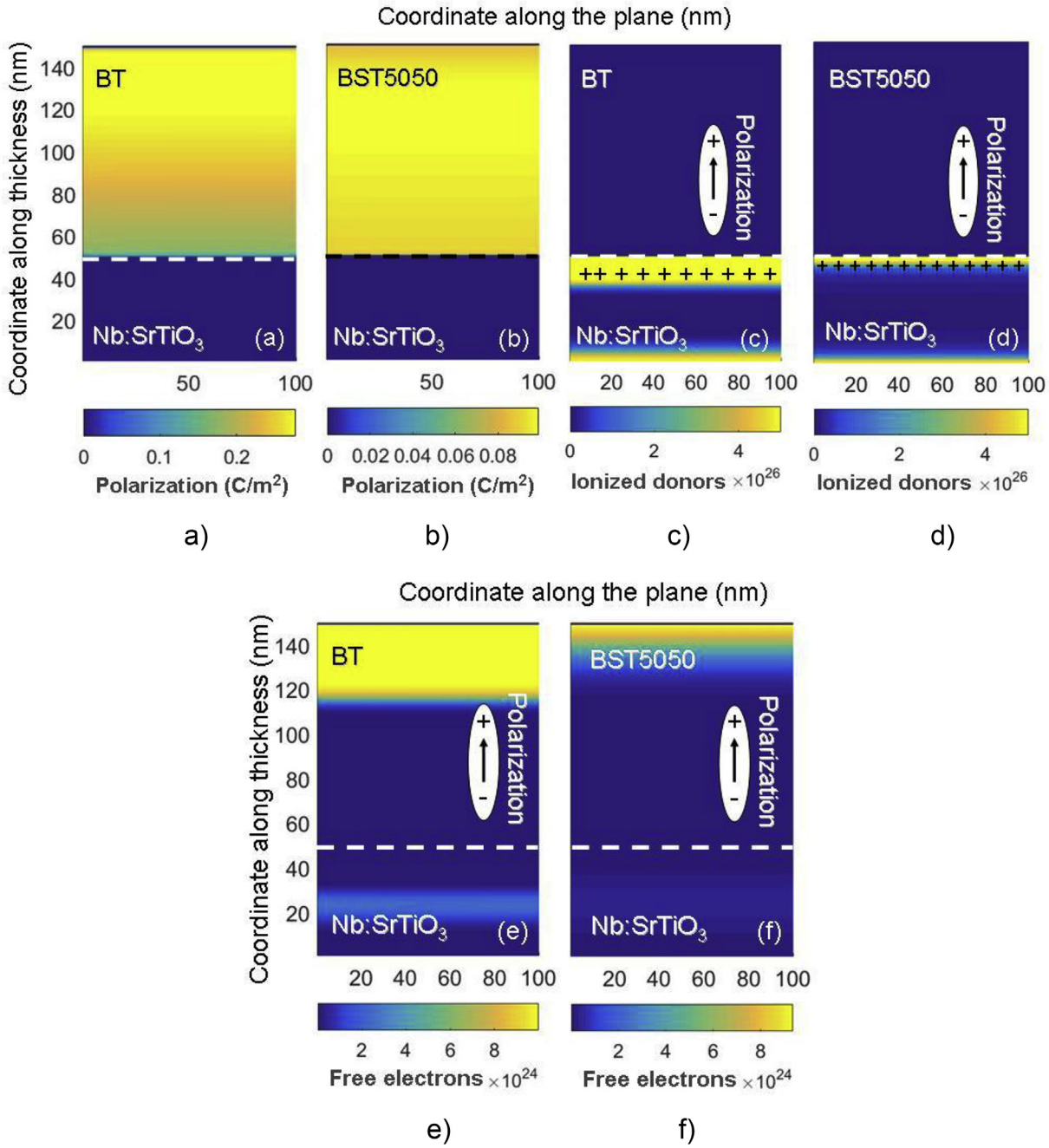

Fig. 8. Polarization and ionized donor maps for BT and BST 5050 films computed from thermodynamic theory to reveal the relation between the polarization strength to the depletion length inside the NSTO under 0 V bias. In (e) and (f) we provide the free carrier densities in the stacks to point out to the accumulation near the top electrode. The colorbar scale for charge density maps has units m^{-3}. Positive (negative) polarization corresponds to the dipoles pointing away (towards) from (to) the NSTO interface.

term denotes “depletion zone” at the NSTO/FE interface on the NSTO side. Fig. 8e and f map the free electron densities inside the BT and BST 5050: Note that the accumulation of the carriers near the top electrode from the FE side is related to the way the polarization terminates at this interface in the presence of the dead layer where one expects significant bound polarization charges (despite the high background polarizability of the Pt lattice [43]). Such accumulation of carriers near electrode interfaces is expected to occur in any ferroelectric film with ionizable impurities and is a phenomena that has been discussed extensively relatively recently in the light of interface boundary conditions [3,4]. Carrier accumulation in the film near the top electrode, combined with the depletion in the NSTO, possibly further favor the imprinted polarization state and stronger the polarization higher the carrier accumulation as given in Fig. 8e–f for BT and BST5050.

A sufficient positive bias on the top Pt electrode (around 1 V for BT and 0.5 V for BST 5050) reverses the above situation, especially following the switching of polarization in both samples (Fig. 9) where the entire stack exhibits free electron accumulation (Fig. 9e and f), causing the high amounts of leakage under positive bias particularly in the BT system. Free electron density is expected to be higher in BT when under positive bias as well as a stronger accumulation of carriers in the NSTO near the bottom interface and therefore a higher leakage current density than the BST 5050 is observed (See Fig. 6 and compare the free electron densities computed and mapped for BT and BST 5050 in Fig. 9e and f). One

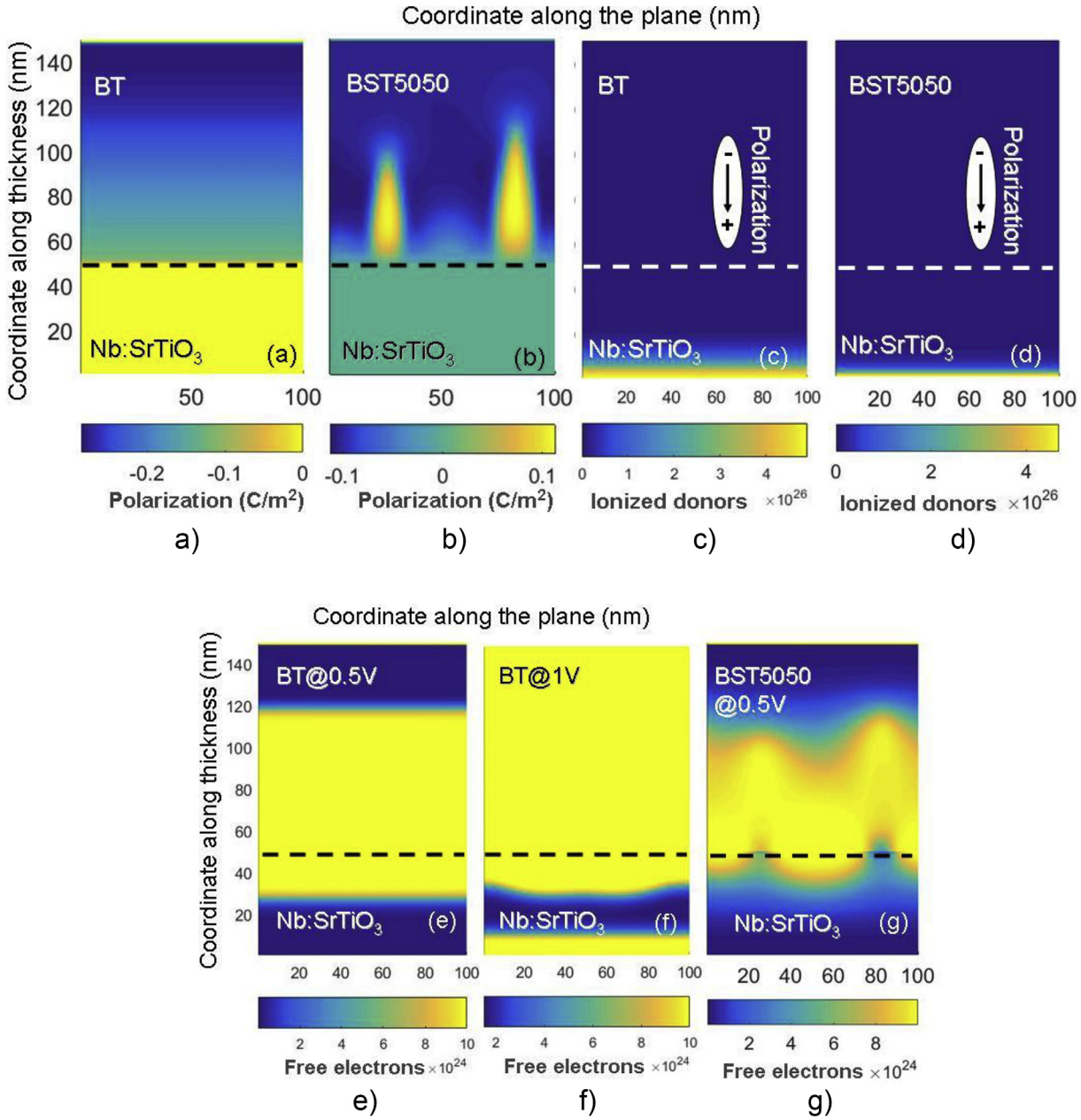

Fig. 9. Polarization and ionized donor maps for BT and BST 5050 films under 0.5 V bias computed from thermodynamic theory to demonstrate the disappearance of the depletion region inside the NSTO that allows conductivity across the thickness of the stack. In (e) and (f) we provide the free carrier densities in the stacks to imply the conductivities expected in BT and BST 5050. Note that we also give here the BT data for 1 V bias for clarity as full switching of BT occurs around 0.8 V while this value is around 0.5 V for BST 5050. The colorbar scale for charge density maps has units m^{-3}. Positive (negative) polarization corresponds to the dipoles pointing away (towards) from (to) the NSTO interface.

can also note that the high resistance − to low resistance transition for BT occurs around 0.75 V (Fig. 6) that is in good agreement with our calculations where we find the electron accumulation in the stack to be significant in our thermodynamic approach.

The flat band energy diagrams are essential here to describe the above phenomena from the view point of the position of the conduction band with respect to the Fermi level. The imprint and the associated carrier distribution can be pictured via use of the computed energy band diagrams given in Fig. 10 where we show the extent of band bending in the presence of the complex electrostatic interactions. Taking the NSTO as a carrier reservoir, yielding a Fermi level of around −4.2 eV (vacuum level being zero), the conduction band of the FE "dips into" the Fermi level near the top interface where carriers accumulate even at zero bias. With increasing positive bias on the top electrode, the entire conduction band is submerged beneath the Fermi level, explaining the positive bias conductivity of the BT and BST 5050 samples in this work. The electrostatic potential due to partially screened polarization charges cause considerable modification to the conduction and the valence bands of the FE films (Fig. 10) and the slope of the conduction band is steeper in BT with respect to that of in the BST 5050 case. Furthermore, the portion of the conduction band near or inside the Fermi level for BT is considerable compared to that of the BST 5050 case (Fig. 10). This is emanating from the difference in the strength of the polarization in the two systems where the stronger polarization in BT generates larger polarization charges upon termination of the dipole sequence at the Pt interface accompanied by the formation of a dead layer there (due to electric field penetration into the Pt). As a result, one can expect carrier accumulation in both BT and BST 5050 near the Pt interface even at zero bias with the former composition having a more prominent impact on this phenomena (Compare Fig. 8e–f and 10). The interpretation of the results of our calculations regarding the conduction band position with respect to the Fermi level of the stacks is pointing out to the bulk controlled conductivity in the experimental measurements on the films. Bulk conductivity here is determined by the extent of the screening of polarization charges at the electrode interfaces, i. e., the band bending inside of the "bulk" of the films is strongly related to the potential drops emanating from the partially screened polarization charges at the interfaces.

One must keep in mind that none of the effects discussed above would have occurred had the electrodes been all ideal where the polarization charges would be perfectly screened, consequently making the electric field inside the FE zero unless the electrode work functions are different. As such, the "resistive switching" process would not have occurred either. The condition of polarization driven "accumulation" and "depletion" at the NSTO/FE interface causes the strong asymmetry in the currents at positive and negative bias observed in the experimental I-V curves of BT and BST 5050 samples. We clearly see from our quasi-static I-V experiments that the leakage currents in BT samples particularly on the positive bias side are at least 2–3 orders of magnitude larger than that of the BST 5050 samples for a given positive bias (Fig. 6b). This observation is entirely in qualitative accordance with our simulations that reveal the NSTO controlled conduction along with bulk conductivity inside the BST films, both driven by polarization strength. The BST 5050, in fact, exhibits this "asymmetry" in a weaker fashion (almost no asymmetry at all for bias < 1 V) owing to its smaller polarization. This is consistent with our thermodynamic calculations where depletion length variations in the NSTO is less for BST 5050 than for BT, hence less of a difference in the currents in the former when under positive and negative bias unless high bias values (approx. >1.5 V) are reached. Thus, one can conclude that the strength of polarization has great influence on the leakage behavior of these systems that arise from the way the polarization interacts with the electrode interfaces and the extent of screening provided by the electrodes for polarization charges. In addition, we find that even if there are no impurities in a ferroelectric film, finite screening of electrodes can alone lead to leakage via bulk conduction inside the FE if the polarization is strong enough (such as in the case of $PbTiO_3$ films).

Having shown that the hystereses in the positive polarity of the samples is due to polarization direction at a given applied bias during an "up" or a "down" bias sweep, one can envision the

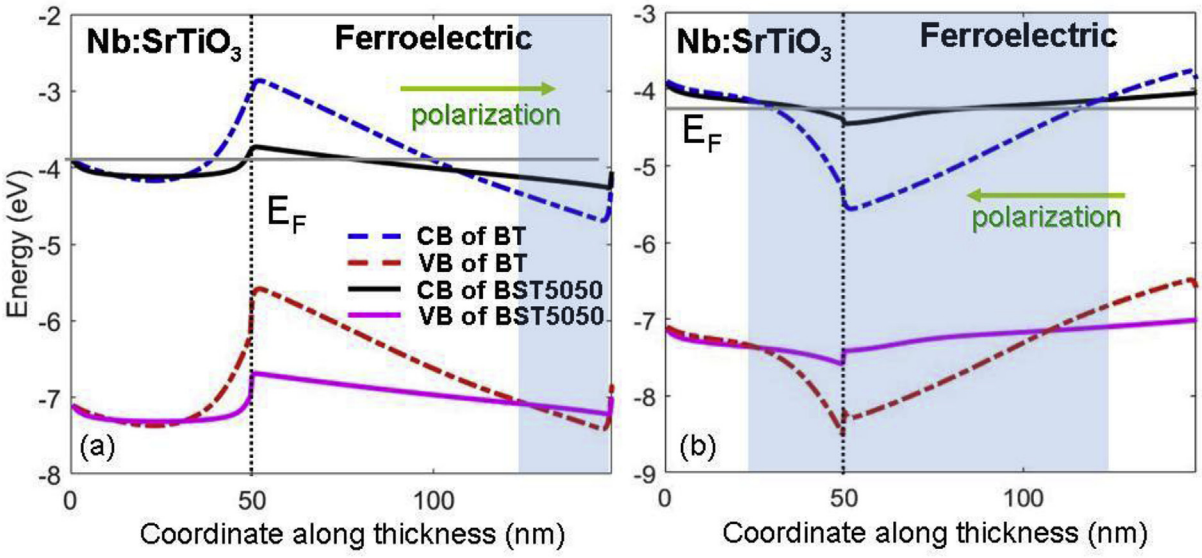

Fig. 10. Flat band energy diagrams computed from thermodynamic theory for (a) BT and BST 5050 when under 0 V bias and (b) when under 0.5 V bias. CB: Conduction band, VB: Valence band. Notice how the CB of BT "submerges" into the Fermi level (E_F) under 0.5 V for this composition (under positive bias). The shaded regions indicate the locations of free electron accumulation. The green arrow in (a) and (b) indicates the direction of polarization. BST 5050 is only slightly influenced by the positive bias with lower conduction currents expected than that of in BT as also observed in experiments. Also note that the energy scales are different in (a) and (b) due the amount of band bending being different in both plots. (For interpretation of the references to color in this figure legend, the reader is referred to the Web version of this article.)

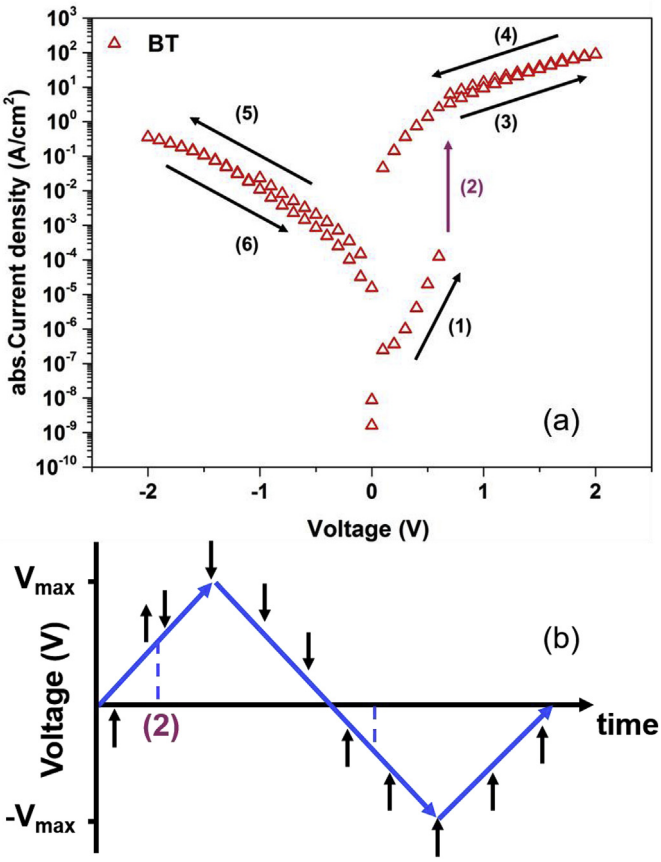

Fig. 11. (a) Plot showing the switching between high-resistance and low-resistance states for the BT films. 1 and 4 correspond to high-resistance and low resistance states respectively during the positive up-sweep and down-sweep. Switching from "up polarization" to "down polarization" occurs at 2. Almost no hysteresis occurs during 5 and 6 as polarization direction in the negative bias is fixed according to our thermodynamic calculation results. (b) Schematic to demonstrate the direction of polarization as deduced from the experiments and thermodynamic calculations. Black arrows imply the polarization direction during the triangular bias-sweep (blue arrows). The vertical blue dashed lines denote the bias values where switching occurs during the sweep. Switching from "down polarization" to "up polarization" occurs at 2 as indicated in (a). (For interpretation of the references to color in this figure legend, the reader is referred to the Web version of this article.)

relation between the triangular bias sweep signal and the polarization direction. In Fig. 11, we help visualize the "high resistance" and "low resistance" portions of the I-V curves taking the quasi-static I-V measurement for the BT sample. Looking at Fig. 11, for the positive bias side of the voltage axis, the shift from high-resistance to low-resistance in the BT film occurs following the passage of the critical bias at which polarization switching occurs confirmed by our thermodynamic simulations. The hysteresis in the BST 5050 film when sweeping the positive bias voltages is not as evident as that of in BT. As we stated, the theoretical result for the critical voltages approximately after which hysteresis effects are recorded are surprisingly coinciding with that of the experimental value (around 0.5 V for BST 5050 and 0.8 V for BT) despite the fact that we do not consider any dynamical effects including nucleation and growth kinetics in our calculations. Moreover, the absence of any detectable hystereses when under negative bias in the quasi-static I-V curves is purely due to the absence of any polarization switching in this regime: the already imprinted "negative polarization" is further enhanced under the negative bias.

Finally, comparing the "hystereses magnitude in the currents" for the 1 kHz measurement and the quasi-static measurement, one can see that the low resistance and high resistance states differ by a few orders of magnitude in both BT and BST 5050 in the latter: We believe that this has to do with the dynamical effects related to polarization relaxation where the 1 kHz measurement might not allow "all regions to switch" under the relatively rapidly varying signal compared to the quasi-static case. Such an effect will diminish the difference between the low resistance and high resistance states for a given bias whose origins have been discussed above. A quasi-static measurement, on the other hand, allows sufficient time for polarization switching and relaxation at every bias step, rendering FE/NSTO interface driven resistive switching more pronounced, hence the significant difference in the currents during the "up-sweep" and "down-sweep" along the positive bias.

5. Conclusions

We discussed the switchable Schottky effect that is accompanied by resistive switching in high quality sol-gel grown BT and BST 5050 thin film samples using experimental and theoretical methods. Analysis of the experimental data in light of the thermodynamic simulations where the FE films are treated as wide bandgap semiconductors explain the asymmetry in the I-V curves and the current hystereses observed under positive bias that is a function of Sr composition. Thermodynamic calculations show that the conductivity of the films under the positive bias will be bulk limited and a strong function of the "polarization strength", that is determined here mostly by the Sr content of the film. The latter claim, in light of the thermodynamic theory, is confirmed by the different amounts of leakage in BT and BST 5050 films particularly in the positive bias regime in the experiments. We show that the "strength" of depletion and accumulation states in the NSTO substrate is a direct function of polarization amplitude. Thus the prominent hysteresis in I-V plots of the BT on the positive bias axis is due to the stronger polarization in these films than in BST 5050. The low leakage under negative bias in the NSTO/FE/Pt stack is controlled by the space charge region in the NSTO under depletion as polarization points away from this interface. Apart from the carrier distribution on the NSTO side of the NSTO/FE interface, the extent of band bending and the carrier concentration in the conduction band of the FE films in bulk-controlled conduction also strongly depends on the strength of polarization and, therefore, is ultimately connected with the effectiveness with which the electrodes screen the polarization charges at the interfaces. Bulk conductivity inside the film occurs when the conduction band of the films enter into the Fermi level when polarization points towards the bottom NSTO substrate (when NSTO is already in accumulation state) away from the top Pt electrode, making the FE a "leaky" film particularly when under positive bias. To explain the effect of polarization on leakage, one is obliged to consider the real nature of the electrodes, i. e., the finite penetration length of the electric field into the electrodes from the FE as it is impossible to explain resistive switching and the hystereses in the I-V curves without this important factor. The hystereses in the I-V curves both in dynamic measurements and quasi-static measurements confirm this mechanism backed up by our thermodynamic simulations. Microstructure is often cited to play a dominant role in thin films as defect sites could give rise to local conductivities and inhomogeneities in the properties of the ferroelectric phase. In our discussions, we did not refer to the possible impact of microstructural features (such as dislocations, defects with inhomogeneous elastic strain fields and etc.) on the results as the major experimental findings here clearly imply the dominant mechanism giving rise to the observed properties to be originating from the electronic character of the film/electrode interfaces. That the theory we applied in this work considers an ideal system yielding results

according with experiment is a direct evidence for this. Our results demonstrate that it is possible to observe and tailor resistive switching in relatively thicker films compared to tunnel junctions where the ferroelectric single domain stability in the latter could be a concern due to size and surface effects.

Acknowledgements

O. M. and I. B. M. acknowledge TÜBİTAK COST Project 113M792 for financial support. G. A. B. and L. P. acknowledge the funding from the Core Program PN16-4801. O. M., C. S. and I. B. M. would like to thank Prof. Mehmet Ali Gulgun of Sabancı University for insight regarding EDX analysis.

Appendix A. Supplementary data

Supplementary data related to this article can be found at https://doi.org/10.1016/j.actamat.2018.02.015.

References

[1] P.W.M. Blom, et al., Ferroelectric schottky diode, Phys. Rev. Lett. 73 (15) (1994) 2107–2110.
[2] K. Abe, et al., Asymmetric ferroelectricity and anomalous current conduction in heteroepitaxial BaTiO3 thin films, Jap. J. Appl. Phys. Part 1-Reg. Pap. Short Not. Rev. Pap. 36 (9B) (1997) 5846–5853.
[3] X.H. Liu, et al., Polarization-controlled Ohmic to Schottky transition at a metal/ferroelectric interface, Phys. Rev. B 88 (16) (2013).
[4] I.B. Misirlioglu, M. Yildiz, Carrier accumulation near electrodes in ferroelectric films due to polarization boundary conditions, J. Appl. Phys. 116 (2) (2014).
[5] L. Pintilie, et al., Polarization induced self-doping in epitaxial Pb(Zr0.20Ti0.80) O-3 thin films, Sci. Rep. 5 (2015).
[6] Y. Watanabe, Tunneling current through a possible all-perovskite oxide p-n junction, Phys. Rev. B 57 (10) (1998) R5563–R5566.
[7] H. Kohlstedt, et al., Theoretical current-voltage characteristics of ferroelectric tunnel junctions, Phys. Rev. B 72 (12) (2005).
[8] M.Y. Zhuravlev, et al., Giant electroresistance in ferroelectric tunnel junctions, Phys. Rev. Lett. 94 (24) (2005).
[9] E.Y. Tsymbal, H. Kohlstedt, Applied physics - tunneling across a ferroelectric, Science 313 (5784) (2006) 181–183.
[10] J.P. Velev, et al., Effect of ferroelectricity on electron transport in Pt/BaTiO3/Pt tunnel junctions, Phys. Rev. Lett. 98 (13) (2007).
[11] A. Gruverman, et al., Tunneling electroresistance effect in ferroelectric tunnel junctions at the nanoscale, Nano Lett. 9 (10) (2009) 3539–3543.
[12] N.A. Zimbovskaya, Electron transport through asymmetric ferroelectric tunnel junctions: current-voltage characteristics, J. Appl. Phys. 106 (12) (2009).
[13] P. Maksymovych, et al., Polarization control of electron tunneling into ferroelectric surfaces, Science 324 (5933) (2009) 1421–1425.
[14] D. Pantel, M. Alexe, Electroresistance effects in ferroelectric tunnel barriers, Phys. Rev. B 82 (13) (2010).
[15] S.D. Ha, S. Ramanathan, Adaptive oxide electronics: a review, J. Appl. Phys. 110 (7) (2011).
[16] M. Bibes, J.E. Villegas, A. Barthelemy, Ultrathin oxide films and interfaces for electronics and spintronics, Adv. Phys. 60 (1) (2011) 5–84.
[17] A. Chanthbouala, et al., Solid-state memories based on ferroelectric tunnel junctions, Nat. Nanotechnol. 7 (2) (2012) 101–104.
[18] D.J. Kim, et al., Ferroelectric tunnel memristor, Nano Lett. 12 (11) (2012) 5697–5702.
[19] A. Chanthbouala, et al., A ferroelectric memristor, Nat. Mater. 11 (10) (2012) 860–864.
[20] X.Y. Lu, H. Li, W.W. Cao, Current-voltage characteristics and ON/OFF ratio in ferroelectric tunnel junctions, J. Appl. Phys. 112 (5) (2012).
[21] D.J. Kim, et al., Retention of resistance states in ferroelectric tunnel memristors, Appl. Phys. Lett. 103 (14) (2013).
[22] Z.H. Wang, et al., Write operation study of Co/BTO/LSMO ferroelectric tunnel junction, J. Appl. Phys. 114 (4) (2013).
[23] E.Y. Tsymbal, A. Gruverman, FERROELECTRIC TUNNEL JUNCTIONS beyond the barrier, Nat. Mater. 12 (7) (2013) 602–604.
[24] Z. Wen, et al., Ferroelectric-field-effect-enhanced electroresistance in metal/ferroelectric/semiconductor tunnel junctions, Nat. Mater. 12 (7) (2013) 617–621.
[25] Y. Fujisaki, Review of emerging new solid-state non-volatile memories, Jpn. J. Appl. Phys. 52 (4) (2013).
[26] R. Soni, et al., Giant electrode effect on tunnelling electroresistance in ferroelectric tunnel junctions, Nat. Commun. 5 (2014).
[27] Z.B. Yan, J.M. Liu, Resistance switching memory in perovskite oxides, Ann. Phys. 358 (2015) 206–224.
[28] H.J. Mao, et al., Unconventional resistive switching behavior in ferroelectric tunnel junctions, Phys. Chem. Chem. Phys. 17 (15) (2015) 10146–10150.
[29] L.X. Zhang, et al., Large resistive switching and switchable photovoltaic response in ferroelectric doped BiFeO3-based thin films by chemical solution deposition, J. Mater. Chem. C 3 (18) (2015) 4706–4712.
[30] M.S. Rahman, et al., Integration of BiFeO3/La0.7Sr0.3MnO3 heterostructures with III-V semiconductors for low-power non-volatile memory and multiferroic field effect transistors, J. Mater. Chem. C 4 (43) (2016) 10386–10394.
[31] Y. Bai, et al., Resistive switching and modulation of Pb(Zr0.4Ti0.6)O-3/Nb: SrTiO3 heterostructures, ACS Appl. Mater. Interfaces 8 (48) (2016) 32948–32955.
[32] A.M. Bratkovsky, A.P. Levanyuk, Smearing of phase transition due to a surface effect or a bulk inhomogeneity in ferroelectric nanostructures, Phys. Rev. Lett. 94 (10) (2005).
[33] Z.G. Ban, S.P. Alpay, Optimization of the tunability of barium strontium titanate films via epitaxial stresses, J. Appl. Phys. 93 (1) (2003) 504–511.
[34] M.B. Okatan, M.W. Cole, S.P. Alpay, Dielectric tunability of graded barium strontium titanate multilayers: effect of thermal strains, J. Appl. Phys. 104 (10) (2008).
[35] M.W. Cole, et al., Dielectric properties of MgO-doped compositionally graded multilayer barium strontium titanate films, Appl. Phys. Lett. 92 (7) (2008).
[36] M.W. Cole, et al., Microwave dielectric properties of graded barium strontium titanate films, Appl. Phys. Lett. 92 (18) (2008).
[37] C.V. Weiss, et al., Compositionally graded ferroelectric multilayers for frequency agile tunable devices, J. Mater. Sci. 44 (19) (2009) 5364–5374.
[38] M. Liu, et al., Interface engineered BaTiO3/SrTiO3 heterostructures with optimized high-frequency dielectric properties, ACS Appl. Mater. Interfaces 4 (11) (2012) 5761–5765.
[39] R.G. Thomas Remmel, Beth Baumert, Characterization of barium strontium titanate using XRD, in: Denver X-ray Conference (DXC) on Applications of X-ray Analysis, 1999.
[40] A.K. Tagantsev, Landau expansion for ferroelectrics: which variable to use? Ferroelectrics 375 (2008) 19–27.
[41] A.P. Levanyuk, B.A. Strukov, A. Cano, Background dielectric permittivity: material constant or fitting parameter? Ferroelectrics 503 (1) (2016) 94–103.
[43] W.S. Choi, et al., Dielectric constants of Ir, Ru, Pt, and IrO2: contributions from bound charges, Phys. Rev. B 74 (20) (2006).
[44] N.A. Pertsev, A.G. Zembilgotov, A.K. Tagantsev, Effect of mechanical boundary conditions on phase diagrams of epitaxial ferroelectric thin films, Phys. Rev. Lett. 80 (9) (1998) 1988–1991.
[45] M.D. Glinchuk, E.A. Eliseev, V.A. Stephanovich, The depolarization field effect on the thin ferroelectric films properties, Phys. B Condens. Matter 322 (3–4) (2002) 356–370.
[46] C.L. Jia, et al., Unit-cell scale mapping of ferroelectricity and tetragonality in epitaxial ultrathin ferroelectric films, Nat. Mater. 6 (1) (2007) 64–69.
[47] L. Pintilie, M. Alexe, Metal-ferroelectric-metal heterostructures with schottky contacts. i. influence of the ferroelectric properties, J. Appl. Phys. 98 (12) (2005).
[48] L. Pintilie, et al., Metal-ferroelectric-metal structures with Schottky contacts. II. Analysis of the experimental current-voltage and capacitance-voltage characteristics of Pb(Zr,Ti)O-3 thin films - art. no. 123104, J. Appl. Phys. 98 (12) (2005).
[49] Y. Xiao, V.B. Shenoy, K. Bhattacharya, Depletion layers and domain walls in semiconducting ferroelectric thin films, Phys. Rev. Lett. 95 (24) (2005).
[50] A. Rana, et al., Scaling behavior of resistive switching in epitaxial bismuth ferrite heterostructures, Adv. Funct. Mater. 24 (25) (2014) 3962–3969.
[51] I.B. Misirlioglu, M. Yildiz, K. Sendur, Domain control of Carrier density at a semiconductor-ferroelectric interface, Sci. Rep. 5 (2015).
[52] N.A. Pertsev, A.K. Tagantsev, N. Setter, Phase transitions and strain-induced ferroelectricity in SrTiO3 epitaxial thin films, Phys. Rev. B 61 (2) (2000) R825–R829.
[53] A.M. Bratkovsky, A.P. Levanyuk, Continuous theory of ferroelectric states in ultrathin films with real electrodes, J. Comput. Theor. Nanosci. 6 (3) (2009) 465–489.